Electronic Research Archive

https://www.aimspress.com/journal/era

ERA, 34(9): 5941–5967.
DOI: 10.3934/era.2026263
Received: 28 April 2026
Revised: 28 June 2026
Accepted: 06 July 2026
Published: 13 July 2026

Research article

Optimal control of patterns toward desired morphologies in a networked reaction-diffusion plankton system

Jiaqi Yang[1], **Ning Li**[1,*] **and Botong Zhang**[2]

[1] College of Sciences, Northeastern University, Shenyang 110819, China
[2] Dongfang Green Energy (Hebei) Co., Ltd., Hebei 061000, China

* **Correspondence:** Email: lining80@163.com.

Abstract: In this paper, we investigated the formation and optimal control of spatial patterns in a plankton ecosystem. Based on a reaction-diffusion model with time delay and cross-diffusion, linear stability analysis revealed the conditions for Turing instability and Hopf oscillations, providing a dynamical explanation for plankton patchiness and periodic red tide outbreaks. A networked reaction-diffusion model was further constructed to account for ecological connectivity. Through global sensitivity analysis, the most influential parameters were identified, and node-dependent control as well as time-dependent optimal control was implemented. Extensive numerical simulations verified that when the network topology and average connectivity varied separately or simultaneously, the proposed control strategy could effectively steer the system toward the target spatial pattern, maintaining the average relative error below 8%. Moreover, the control method could significantly reduce system deviations in the short term, thereby effectively mitigating the adverse effects of time delay. This work provides a quantitative framework for understanding and regulating spatial heterogeneity in plankton ecosystems, with potential implications for red tide management.

Keywords: networks; reaction-diffusion; Turing pattern; global sensitivity analysis; optimal control

1. Introduction

In recent decades, under the combined pressures of anthropogenic disturbance [1] and climate change [2], the dynamic response and stability maintenance of phytoplankton communities have become important topics in ecological research. In the natural environment, the distribution and migration of plankton are regulated by spatial factors such as water flow, diffusion, and environmental fluctuations [3–5]. Futhermore, its physiological processes, adaptive responses, and population feedback often involve pronounced time-delay effects [6, 7]. The coupling between diffusion and delay drives plankton ecosystems to exhibit rich spatiotemporal dynamic behaviors, such as pattern

formation, oscillatory phenomena and traveling wave propagation. Among these phenomena, Turing patterns [8–10] not only reveal the internal dynamics of the system, but are also closely related to the functional stability of the ecosystem. However, it remains a challenge to identify key regulatory indicators from complex dynamics and to design practical and effective rapid intervention strategies for red tide prevention and control.

Although plankton systems have attracted widespread attention in the field of theoretical ecology [11–15], researchers focus on model construction and dynamic analysis. For example, the researchers in [15] studied the interaction of toxic phytoplankton with zooplankton based on ordinary differential equations; the researchers in [11] established a stochastic plankton model including Markov switches and pulsed pollution. The researchers in [12] analyzed non-voluntary stochastic systems containing toxin-producing phytoplankton and pulsed perturbations. The researchers in [13] used the reaction diffusion model to explore the spatiotemporal dynamics near the Turing-Hopf bifurcation. The researchers in [14] investigated plankton models with seasonality and vegetation shelter. While these studies have made significant progress, a major challenge arises when moving from dynamic analysis to control implementation: The trade-off between model realism and mathematical tractability. Moreover, including more environmental and biological factors to reflect real-world conditions inevitably increases the complexity of the equations, which often makes the analytical derivation of optimal control laws extremely difficult.

In constructing the spatiotemporal pattern model of ecosystems, the classical reaction diffusion [16] theory provides a basic framework for understanding the dynamic relationship between populations and the environment. However, the actual ecological environment often does not have the ideal characteristics of continuous uniformity, but instead presents network structural characteristics, such as complex networks formed by hydrological connectivity [17], nutrient transport [18], and biological migration [19]. Therefore, the Turing model based on the network response diffusion system can more accurately reflect the heterogeneity and connectivity of a networked ecosystem. By abstracting habitats into network structures and analyzing them in combination with node and edge properties, the aggregation and dispersal potential of plankton and nutrients can be quantified, thereby identifying key areas and sensitive periods for red tides. Network topology analysis has been widely applied to SIR epidemic models [20, 21] for epidemic prevention and control and information dissemination [17–20, 22]. In particular, network frameworks have achieved high maturity, integrating intelligent algorithms for data-driven propagation analysis [21] or optimizing control under strict capacity constraints [23]. These approaches are designed for the suppression of population spread at the node level, which differs from the research focus on spatiotemporal pattern regulation in plankton ecosystems.

Despite these challenges, several studies have begun to bridge theoretical analysis and practical regulation. For example, delay-feedback control for delayed predator–prey or plankton-like systems [24] and hybrid control for reaction-diffusion marine plankton ecosystems [25] illustrate the feasibility of active intervention. However, these studies mainly entail mechanism simulation and theoretical control, and have not been deeply integrated into ecological management practice, nor have they provided specific strategies for red tide prevention and control. Unlike conventional control approaches, we develop a sensitivity-guided framework that directly targets the dominant pattern-forming parameters, enabling efficient regulation of spatiotemporal dynamics in delayed networked ecosystems. This method provides a quantifiable and universal theoretical tool for red tide

prevention and control and makes up for the shortcomings of the theoretical model in research.

Considering the strengths and limitations of current research, together with the above studies, the major contributions of this study are summarized as follows.

1) A plankton ecological model with time delay and cross-diffusion is established. It captures delayed biological responses and asymmetric diffusion, enabling a better description of the spatiotemporal dynamics related to red tides.
2) Network reaction-diffusion theory is introduced to describe plankton dynamics. By modeling habitats as heterogeneous networks instead of continuous media, the approach reflects spatial patchiness and connectivity more realistically. Based on this, an optimal control framework is used to guide the system toward desired spatial patterns.
3) An optimal control method based on global sensitivity analysis (GSA) is proposed. The method identifies key parameters affecting the amplitude of spatial patterns calculated via the Fast Fourier Transform (FFT) and dynamically adjusts the weights of control variables. It enables efficient regulation toward the target pattern with reduced control cost and mitigates the adverse effects of time delay.

2. Model formulation

To describe the interaction between phytoplankton and zooplankton in a spatial environment, we consider a delayed reaction–diffusion system with self-diffusion and cross-diffusion terms. This type of formulation has been used in related studies on plankton dynamics and delayed predator–prey systems [25]. The model is given by

$$\begin{cases} \dfrac{\partial P(t,x)}{\partial t} = d_{11}\Delta P(t,x) + d_{12}\Delta Z(t,x) + r_1 P(t,x)\left(1 - \dfrac{P(t,x)}{\delta}\right) - mf(P(t,x))Z(t-\tau_1,x), \\ \dfrac{\partial Z(t,x)}{\partial t} = d_{21}\Delta P(t,x) + d_{22}\Delta Z(t,x) + r_2 Z(t,x)\left(1 - \dfrac{Z(t,x)}{\gamma P(t-\tau_2,x)}\right), \\ \qquad\qquad t > 0,\ x \in \Omega. \end{cases} \tag{2.1}$$

The boundary is assumed to satisfy homogeneous Neumann conditions,

$$\frac{\partial P(t,x)}{\partial \nu} = \frac{\partial Z(t,x)}{\partial \nu} = 0, \qquad t > 0,\ x \in \partial\Omega,$$

and the initial data are taken as

$$\begin{cases} P(t,x) = \phi_1(t,x) \geq 0, \\ Z(t,x) = \phi_2(t,x) \geq 0, \end{cases} \qquad (t,x) \in [-\tau, 0] \times \overline{\Omega}.$$

Here, $(\phi_1, \phi_2)^\top \in C := C([-\tau, 0], X)$, where

$$X = \left\{ (P,Z) :\ P, Z \in W^{2,2}(\Omega),\ \frac{\partial P(t,x)}{\partial \nu} = \frac{\partial Z(t,x)}{\partial \nu} = 0,\ x \in \partial\Omega \right\},$$

and the inner product in X is denoted by $\langle \cdot, \cdot \rangle$.

The variables $P(t,x)$ and $Z(t,x)$ represent the densities of phytoplankton and zooplankton, respectively. The operator Δ is the Laplacian in $\mathbb{R}^n$. The coefficients d_{11} and d_{22} stand for self-diffusion, while d_{12} and d_{21} describe cross-diffusion effects. Throughout the paper, we assume that $\Omega = (0, \ell\pi)$ with $\ell > 0$, where $\partial\Omega$ is smooth and ν is the outward unit normal vector on the boundary. Under the Neumann condition, no population flux passes through the boundary, so the habitat can be regarded as closed.

Table 1. Definitions of model parameters.

Symbol	Meaning
r_1	Endogenous growth rate of phytoplankton
r_2	Endogenous growth rate of zooplankton
δ	Environmental carrying capacity for phytoplankton
γ	Nutritional value of phytoplankton for zooplankton
γP	Carrying capacity of phytoplankton for zooplankton
m	Predation rate of zooplankton on phytoplankton
$f(P)$	Functional response function
τ_1	Maturation delay of the zooplankton
τ_2	Delayed feedback of the phytoplankton
τ	Total time delay ($\tau = \tau_1 + \tau_2$)
d_{11}	Self-diffusion coefficient of phytoplankton
d_{22}	Self-diffusion coefficient of zooplankton
d_{12}	Cross-diffusion coefficient of phytoplankton to zooplankton
d_{21}	Cross-diffusion coefficient of zooplankton to phytoplankton
a	Half-saturation constant

The biological meanings of the parameters are listed in Table 1. In addition, we suppose that $a < \delta$, $\tau r_2 < 1$, and $d_{11}d_{22} > d_{12}d_{21}$, which are consistent with the biological background considered here.

If all diffusion terms are removed, then system (2.1) degenerates into a temporal plankton interaction model without spatial effects [26, 27]. In this work, however, the spatial part is important because our goal is not only to study coexistence, but also to investigate how spatial structures arise and how they may be guided toward a desired pattern. To keep the mathematical analysis tractable, we treat the formulation as a reasonable modeling approximation by employing the total lumped time delay $\tau = \tau_1 + \tau_2$ [25]. Under this simplification, system (2.1) is reduced to the following single-delay model

$$\begin{cases} \dfrac{\partial P(t,x)}{\partial t} = d_{11}\Delta P(t,x) + d_{12}\Delta Z(t,x) + r_1 P(t,x)\left(1 - \dfrac{P(t,x)}{\delta}\right) - mf(P(t,x))Z(t-\tau,x), \\ \dfrac{\partial Z(t,x)}{\partial t} = d_{21}\Delta P(t,x) + d_{22}\Delta Z(t,x) + r_2 Z(t,x)\left(1 - \dfrac{Z(t,x)}{\gamma P(t,x)}\right), \\ \qquad\qquad t > 0,\ x \in \Omega. \end{cases} \tag{2.2}$$

Throughout this paper, the response function is assumed to satisfy

$$(H1) \qquad f(0) = 0, \qquad f'(x) > 0 \text{ for } x \geq 0, \qquad \lim_{x\to\infty} f(x) = 1.$$

This condition covers the usual response functions used in plankton and predator–prey models. In particular, the Holling type II case will be adopted in the numerical section.

Theorem 1. *With the assumptions above, if (H1) holds, system* (2.2) *has a unique positive equilibrium* $E^* = (P^*, Z^*)$*, where* P^* *is the unique positive solution of* $\delta m\gamma f(P^*) = r_1(\delta - P^*)$*, and* $Z^* = \gamma P^*$.

Proof. To find the spatially homogeneous positive equilibrium $E^* = (P^*, Z^*)$, we set the time derivatives and spatial diffusion terms in system (2.2) to zero($\Delta P = \Delta Z = 0$), yielding the algebraic equations

$$r_1 P\left(1 - \frac{P}{\delta}\right) - mf(P)Z = 0, \quad r_2 Z\left(1 - \frac{Z}{\gamma P}\right) = 0.$$

For a positive equilibrium, the second equation gives $Z = \gamma P$. Substituting this into the first equation and dividing by $P > 0$, we obtain $r_1(1 - P/\delta) - m\gamma f(P) = 0$, which algebraically rearranges to $\delta m\gamma f(P) - r_1(\delta - P) = 0$. Define $G(P) = \delta m\gamma f(P) - r_1(\delta - P)$. By (H1), it has $G(0) = -r_1\delta < 0, G'(P) = \delta m\gamma f'(P) + r_1 > 0$. Hence, $G(P)$ is strictly increasing on $[0, \infty)$. It follows that $G(P) = 0$ has exactly one positive solution, which determines P^*. Then Z^* is uniquely given by $Z^* = \gamma P^*$.

Therefore, system (2.2) has a unique positive equilibrium $E^* = (P^*, Z^*)$.

3. Linear stability analysis

We study the local behavior of system (2.2) around the positive equilibrium $E^* = (P^*, Z^*)$. Introduce small perturbations

$$P(t, x) = P^* + u(t, x), Z(t, x) = Z^* + v(t, x). \tag{3.1}$$

Then the delayed variable can be written as $Z(t - \tau, x) = Z^* + v(t - \tau, x)$.

Substituting these expressions into system (2.2) and keeping only linear terms, we obtain

$$\begin{pmatrix} \dfrac{\partial u(t,x)}{\partial t} \\ \dfrac{\partial v(t,x)}{\partial t} \end{pmatrix} = D\Delta \begin{pmatrix} u(t,x) \\ v(t,x) \end{pmatrix} + A \begin{pmatrix} u(t,x) \\ v(t,x) \end{pmatrix} + B \begin{pmatrix} u(t-\tau,x) \\ v(t-\tau,x) \end{pmatrix}, \tag{3.2}$$

where

$$D = \begin{pmatrix} d_{11} & d_{12} \\ d_{21} & d_{22} \end{pmatrix}, \qquad A = \begin{pmatrix} a_{11} & 0 \\ a_{21} & a_{22} \end{pmatrix}, \qquad B = \begin{pmatrix} 0 & b \\ 0 & 0 \end{pmatrix},$$

with

$$a_{11} = r_1 - \frac{2r_1P^*}{\delta} - m\gamma P^* f'(P^*), \qquad a_{21} = r_2\gamma, \qquad a_{22} = -r_2, \qquad b = -mf(P^*).$$

The matrix D comes from diffusion, A is associated with the instantaneous reaction terms, and B represents the delayed contribution.

To derive the characteristic equation, we look for modal solutions in the form

$$\begin{pmatrix} u(t,x) \\ v(t,x) \end{pmatrix} = e^{\lambda t}\cos(kx)\begin{pmatrix} c_1 \\ c_2 \end{pmatrix},$$

where c_1 and c_2 are arbitrary constants representing the initial amplitudes of the perturbations for phytoplankton (P) and zooplankton (Z), respectively.

Since the eigenvalues of Δ on X under the Neumann condition are $-k^2$ for $k \in \mathbb{N}_0 := \{0, 1, 2, \ldots\}$, the characteristic equation of the linearized system is

$$\det\left[\lambda I + k^2 D - A - Be^{-\lambda\tau}\right] = 0.$$

Equivalently,

$$\det\begin{pmatrix} \lambda + d_{11}k^2 - a_{11} & d_{12}k^2 - be^{-\lambda\tau} \\ d_{21}k^2 - a_{21} & \lambda + d_{22}k^2 - a_{22} \end{pmatrix} = 0,$$

where I is the identity matrix of order two. Thus, the characteristic equation can be written as

$$\lambda^2 + T(k)\lambda + W(k, \lambda) = 0, \tag{3.3}$$

where

$$T(k) = (d_{11} + d_{22})k^2 - (a_{11} + a_{22}), \tag{3.4}$$

$$W(k, \lambda) = (d_{11}k^2 - a_{11})(d_{22}k^2 - a_{22}) - d_{12}k^2(d_{21}k^2 - a_{21}) + be^{-\lambda\tau}(d_{21}k^2 - a_{21}). \tag{3.5}$$

For ecological competition networks, constructing an explicit Lyapunov function remains a challenging problem, and global bifurcation analysis based on fully nonlinear methods is often intractable. Hence, linearization is commonly used to study local bifurcation behavior [10, 13, 20, 22, 28] and is adopted here.

We next examine the Turing instability of the positive equilibrium $E^* = (P^*, Z^*)$ without delay, followed by the Hopf bifurcation induced by time delay.

3.1. Turing instability without time delay ($\tau = 0$)

When $\tau = 0$, the characteristic equation (3.3) reduces to

$$\lambda^2 + T(k)\lambda + W(k) = 0, \tag{3.6}$$

where

$$T(k) = (d_{11} + d_{22})k^2 - (a_{11} + a_{22}), \tag{3.7}$$

and

$$W(k) = \det(D)k^4 - (d_{22}a_{11} + d_{11}a_{22} - d_{12}a_{21} - bd_{21})k^2 + (a_{11}a_{22} - ba_{21}), \tag{3.8}$$

with $\det(D) = d_{11}d_{22} - d_{12}d_{21}$. We assume the following conditions:

(H2) $a_{11} + a_{22} < 0, \quad a_{11}a_{22} - ba_{21} > 0.$

(H3) $d_{22}a_{11} + d_{11}a_{22} - d_{12}a_{21} - bd_{21} > 0.$

(H4) $(d_{22}a_{11} + d_{11}a_{22} - d_{12}a_{21} - bd_{21})^2 > 4\det(D)(a_{11}a_{22} - ba_{21}).$

Case A. No time delay with no diffusion.

Theorem 2. *Assume that $d_{11} = d_{12} = d_{21} = d_{22} = 0$ and $\tau = 0$. If (H2) holds, then the positive equilibrium $E^* = (P^*, Z^*)$* of system (2.2) is locally asymptotically stable.

Proof. Under the given conditions, (3.6) reduces to $\lambda^2 - (a_{11} + a_{22})\lambda + (a_{11}a_{22} - ba_{21}) = 0$. The Routh–Hurwitz conditions are satisfied, and all roots have negative real parts.

Case B. No time delay with diffusion.

Theorem 3. *Assume $d_{11}, d_{12}, d_{21}, d_{22} > 0$, $\det(D) > 0$, and $\tau = 0$. If (H2)–(H4) hold, then the positive equilibrium $E^* = (P^*, Z^*)$ undergoes Turing bifurcation.*

Proof. Let $q = k^2 \geq 0$ and define $G(q) = \det(D)q^2 - (d_{22}a_{11} + d_{11}a_{22} - d_{12}a_{21} - bd_{21})q + (a_{11}a_{22} - ba_{21})$. By (H2), we have $G(0) > 0$ and $T(k) > 0$ for all $k \geq 0$. Furthermore, (H3) implies that the linear coefficient of $G(q)$ is negative, and (H4) guarantees that the discriminant of $G(q)$ is positive. Therefore, $G(q)$ is a convex quadratic with $G(0) > 0$, a positive vertex, and a negative minimum value. Consequently, there exist $q > 0$ such that $G(q) < 0$, $W(k) < 0$ for some $k \neq 0$. Moreover, since $T(k) > 0$ for all k, the characteristic equation $\lambda^2 + T(k)\lambda + W(k) = 0$ has a root with positive real part for those wavenumbers, while for $k = 0$, the equilibrium remains stable. This is exactly the Turing instability.

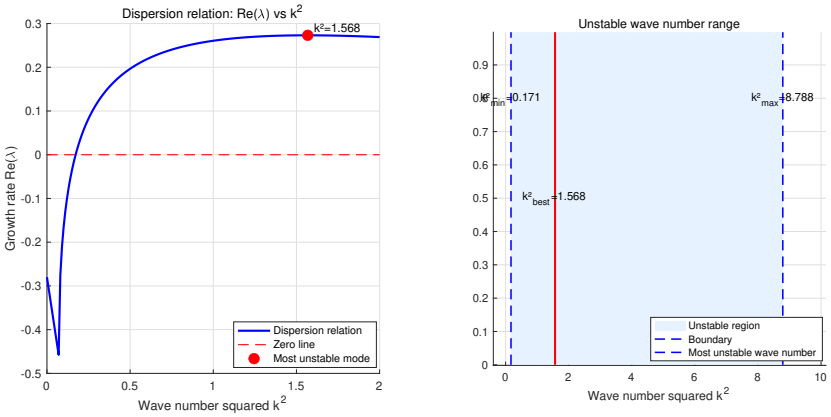

Figure 1. Dispersion relation and unstable wave-number interval for the plankton reaction–diffusion model.

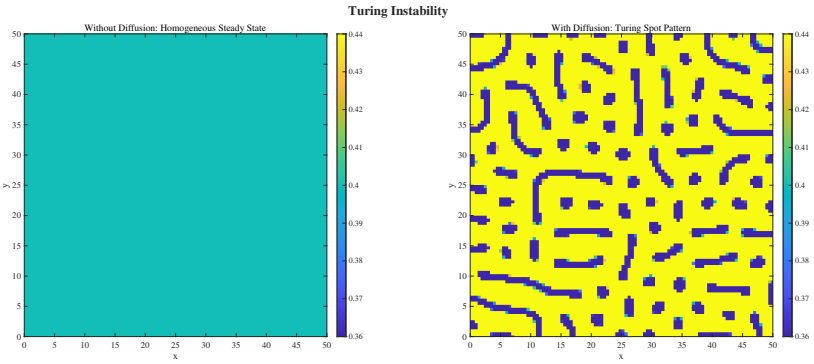

Figure 2. Spatial dynamics of the plankton model with and without diffusion. Left: homogeneous steady state in the absence of diffusion. Right: Diffusion-driven Turing spot pattern when diffusion is present.

For numerical illustration, we choose $r_1 = 1.0, r_2 = 1.0, \delta = 2.0, \gamma = 1.0, m = 1.0, a = 0.1, d_{11} = 0.05, d_{12} = 0.1, d_{21} = 0.1, d_{22} = 5.0$. Under these values, the positive equilibrium is $E^* = (0.4, 0.4)$.

The numerical results in Figures 1 and 2 show the same conclusion. Without diffusion, the solution stays spatially uniform. Once diffusion is introduced, a stationary heterogeneous pattern emerges. This indicates that the spatial pattern is generated by diffusion-driven instability.

3.2. Hopf bifurcation analysis with time delay

Now turn to the delayed case. For convenience, define

$$J_{11}(k) = a_{11} - d_{11}k^2, \qquad J_{22}(k) = a_{22} - d_{22}k^2, \qquad J_{21}(k) = a_{21} - d_{21}k^2.$$

Suppose that $i\omega$ with $\omega > 0$ is a root of (3.3). Then

$$-\omega^2 - i\omega(J_{11} + J_{22}) + J_{11}J_{22} = bJ_{21}(\cos\theta - i\sin\theta) - d_{12}k^2J_{21}, \qquad \theta = \omega\tau.$$

Comparing the real and imaginary parts gives

$$\begin{cases} -\omega^2 + J_{11}J_{22} = bJ_{21}\cos\theta - d_{12}k^2J_{21}, \\ \omega(J_{11} + J_{22}) = bJ_{21}\sin\theta. \end{cases}$$

Hence,

$$\sin\theta = \frac{\omega(J_{11} + J_{22})}{bJ_{21}}, \qquad \cos\theta = \frac{-\omega^2 + J_{11}J_{22} + d_{12}k^2J_{21}}{bJ_{21}}. \tag{3.9}$$

Using $\sin^2\theta + \cos^2\theta = 1$, we obtain

$$[\omega(J_{11} + J_{22})]^2 + [-\omega^2 + J_{11}J_{22} + d_{12}k^2J_{21}]^2 = (bJ_{21})^2.$$

Let

$$\Omega = \omega^2.$$

Then Ω satisfies

$$\Omega^2 + B(k)\Omega + C(k) = 0, \tag{3.10}$$

where

$$B(k) = (J_{11} + J_{22})^2 - 2(J_{11}J_{22} + d_{12}k^2J_{21}),$$
$$C(k) = (J_{11}J_{22} + d_{12}k^2J_{21})^2 - (bJ_{21})^2.$$

Assume that (3.10) has a positive root $\Omega^* > 0$, and write

$$\omega_0 = \sqrt{\Omega^*}.$$

Then the critical values of the delay are

$$\tau_n(k) = \frac{1}{\omega_0}\left[\arccos\left(\frac{\omega_0^2 - J_{11}J_{22} - d_{12}k^2J_{21}}{bJ_{21}}\right) + 2n\pi\right], \qquad n = 0, 1, 2, \ldots. \tag{3.11}$$

Define

$$\tau_0 = \min_{k\in K,\, n\geq 0} \tau_n(k), \qquad \omega_0 = \omega(k_0),$$

where $k_0 \in K$ is the wave number at which the minimum is attained. To determine whether the purely imaginary eigenvalues $\pm i\omega_0$ cross the imaginary axis with non-zero speed at $\tau = \tau_0$, we examine the transversality condition. Let $\lambda(\tau) = \beta(\tau) + i\omega(\tau)$ be a root of the characteristic equation such that $\beta(\tau_0) = 0$ and $\omega(\tau_0) = \omega_0$.

Differentiating the characteristic (3.3) implicitly with respect to τ yields:

$$(2\lambda - J_{11} - J_{22})\frac{d\lambda}{d\tau} - bJ_{21}e^{-\lambda\tau}\left(-\tau\frac{d\lambda}{d\tau} - \lambda\right) = 0.$$

Rearranging the terms, we obtain the expression for $\left(\frac{d\lambda}{d\tau}\right)^{-1}$:

$$\left(\frac{d\lambda}{d\tau}\right)^{-1} = \frac{2\lambda - J_{11} - J_{22}}{-\lambda bJ_{21}e^{-\lambda\tau}} - \frac{\tau}{\lambda} = \frac{-(2\lambda - J_{11} - J_{22})e^{\lambda\tau}}{bJ_{21}\lambda} - \frac{\tau}{\lambda}.$$

Substituting $\lambda = i\omega_0$ and $\tau = \tau_0$ into the above equation, and noting that the second term $-\frac{\tau_0}{i\omega_0} = i\frac{\tau_0}{\omega_0}$ is purely imaginary, we take the real part of the first term using $e^{i\omega_0\tau_0} = \cos(\omega_0\tau_0) + i\sin(\omega_0\tau_0)$:

$$\mathrm{Re}\left[\left(\frac{d\lambda}{d\tau}\right)^{-1}\right]_{\tau=\tau_0} = \frac{-2\omega_0\cos(\omega_0\tau_0) + (J_{11} + J_{22})\sin(\omega_0\tau_0)}{bJ_{21}\omega_0}.$$

By substituting the expressions for $\sin(\omega_0\tau_0)$ and $\cos(\omega_0\tau_0)$ from (3.9) into this equation, the real part can be simplified into the following elegant polynomial form:

$$\mathrm{Re}\left[\left(\frac{d\lambda}{d\tau}\right)^{-1}\right]_{\tau=\tau_0} = \frac{2\omega_0^2 + B(k_0)}{b^2J_{21}^2}. \tag{3.12}$$

Since $\mathrm{sign}\left\{\mathrm{Re}\left(\frac{d\lambda}{d\tau}\right)\right\} = \mathrm{sign}\left\{\mathrm{Re}\left(\frac{d\lambda}{d\tau}\right)^{-1}\right\}$, we introduce the following simplified transversality hypothesis:

$$\text{(H5)} \quad 2\omega_0^2 + B(k_0) \neq 0.$$

Theorem 4. Assume that equilibrium E^* is locally asymptotically stable when $\tau = 0$, that there exists a wave number $k_0 \in K$ such that $\tau_0 = \min_{k\in K}\tau_0(k)$ with the corresponding $\omega_0 > 0$, and that the transversality condition (*H*5) holds. Then the following statements are true:

(i) For $\tau \in [0, \tau_0)$, E^* is locally asymptotically stable.
(ii) At $\tau = \tau_0$, a Hopf bifurcation occurs at E^*; a family of small-amplitude periodic solutions bifurcates from E^*.
(iii) For $\tau > \tau_0$ sufficiently close to τ_0, E^* becomes unstable and stable periodic oscillations arise.

Proof. By definition of τ_0 and the second assumption, the characteristic equation has a pair of purely imaginary eigenvalues $\pm i\omega_0$ at $\tau = \tau_0$. The first assumption together with the minimality of τ_0 implies that all eigenvalues have negative real parts for $\tau < \tau_0$; at $\tau = \tau_0$, the remaining eigenvalues still have negative real parts (non-degenerate case). The third assumption guarantees that the conjugate pair crosses the imaginary axis with non-zero speed. Hence, by the Hopf bifurcation theorem for delay differential equations, conclusions follow.

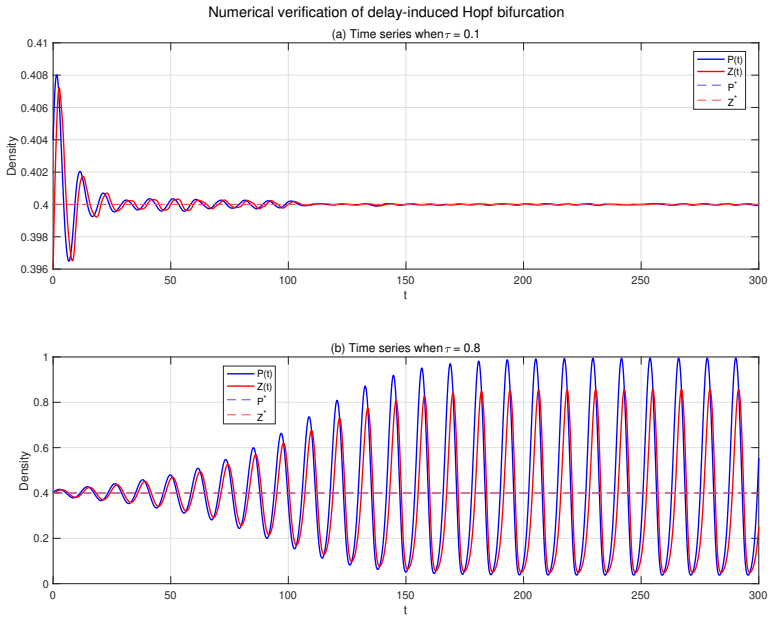

Figure 3. Time series for different delay values. Convergence to equilibrium for small τ and sustained oscillations for larger τ, illustrating delay-induced Hopf bifurcation.

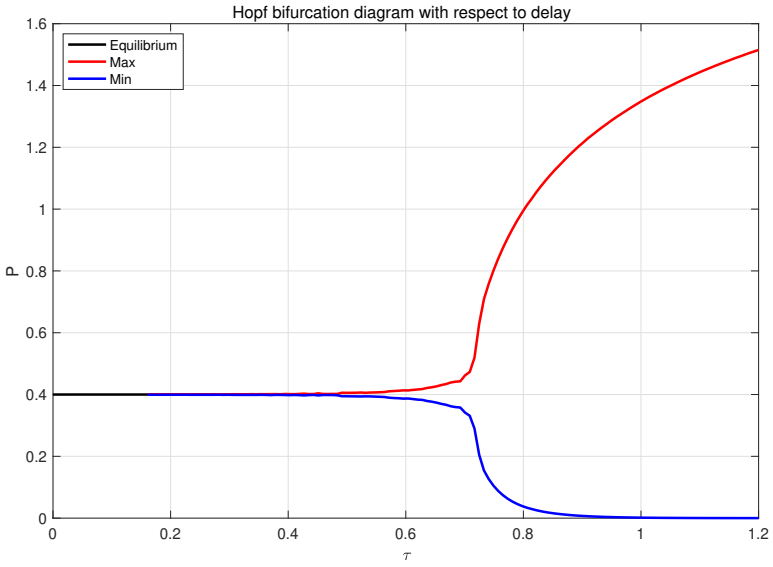

Figure 4. Hopf bifurcation diagram with respect to the delay τ. The red and blue curves denote the maxima and minima of $P(t)$, respectively.

Using the same parameter values as in the Turing case, we further illustrate the effect of the delay. The time series corresponding to $\tau = 0.1$ and $\tau = 0.8$ are shown in Figure 3. For small delay, the solution converges to the equilibrium, while for larger delay, persistent oscillation appears. This agrees with the Hopf bifurcation analysis. The corresponding bifurcation diagram is shown in Figure 4.

4. Sensitivity analysis

Based on the results of the linear stability analysis of the system, in this section, we systematically explain the influence of each parameter on the spatiotemporal dynamics of a plankton ecosystem through GSA [29, 30]. To quantitatively characterize the effect of parameter perturbations on the spatial heterogeneity of the system, the variance-based Sobol GSA is adopted in this paper, which requires a single scalar evaluation index as input. For this purpose, the two-dimensional FFT [31] is introduced to transform the steady-state phytoplankton density distribution into the wavenumber domain. The peak amplitude corresponding to the dominant wavenumber is extracted, based on which the mathematical definition of spatial pattern amplitude is proposed. Ecologically, this amplitude can directly reflect the manifestation intensity of Turing patterns and accurately quantify the severity of spatial heterogeneity phenomena such as red tide outbreaks.

In the control design, priority should be given to highly sensitive parameters, and their small changes can significantly change the formed spatio-temporal pattern. Table 2 lists the parameters analyzed and their numerical ranges. The parameter ranges are selected based on commonly used values in plankton ecosystem models and reaction–diffusion systems with delay and cross-diffusion [32].

Table 2. Parameter ranges used in GSA.

Parameter	Values	Reference
r_1	$0.5 \sim 1.5$	[25, 27]
r_2	$0.5 \sim 1$	[25, 26]
δ	2	[25]
γ	1	*assumed*
m	1	[25, 27]
τ	0.3	[6, 7]
d_{11}	$0.05 \sim 0.20$	[13, 33]
d_{22}	5	*assumed*
d_{12}	$0.10 \sim 0.20$	[13, 33]
d_{21}	$0.08 \sim 0.12$	[33]
a	$0.1 \sim 1$	[26]

For the functional response, we adopt the Holling type II form $f(P) = \frac{P}{a+P}$, which is widely used in plankton interaction models [34–37].

The variance-based Sobol method decomposes the total variance of the model output (mode amplitude A), denoted as $V(A)$, into fractions attributable to individual parameters and their interactions.

The first-order sensitivity index S_i measures the independent, direct contribution of parameter p_i to the output variance:

$$S_i = \frac{V_{p_i}(E_{\mathbf{p}_{\sim i}}(A|p_i))}{V(A)} \tag{4.1}$$

where $\mathbf{p}_{\sim i}$ denotes the vector of all parameters except p_i, $E_{\mathbf{p}_{\sim i}}(\cdot)$ represents the expectation taken over $\mathbf{p}_{\sim i}$, and $V_{p_i}(\cdot)$ is the variance taken over p_i.

To explicitly account for non-linear couplings, the total-effect index S_{T_i} measures the overall contribution of p_i, encompassing its first-order effect and all higher-order interactions:

$$S_{T_i} = 1 - \frac{V_{\mathbf{p}_{\sim i}}(E_{p_i}(A|\mathbf{p}_{\sim i}))}{V(A)} \tag{4.2}$$

where $E_{p_i}(\cdot)$ is the expectation taken over p_i, and $V_{\mathbf{p}_{\sim i}}(\cdot)$ is the variance taken over all parameters except p_i.

In the numerical simulations, the spatiotemporal model is solved by discretizing space via the finite difference method and performing time integration using the explicit Euler method, with the delay term handled by storing historical state values. Based on this numerical solver, the sensitivity indices are efficiently computed using the standard Saltelli sampling scheme. This requires a total of $N(d + 2)$ model runs, where N is the base sample size and d is the total number of input parameters. The key parameters, together with their resulting sensitivity indices and interaction effects, are presented in Figure 5. The convergence analysis of the Sobol sensitivity indices is presented in Figure 6.

The sensitivity analysis in this section provides a mathematical clarity of regulatory priorities. As visualized in Figure 5, the phytoplankton self-diffusion coefficient d_{11} shows the strongest total effect ($S_T = 0.902$) and a substantial first-order effect ($S_1 = 0.583$), making it the dominant independent factor. For the growth rates of both populations (r_1 and r_2), their interaction effects (0.280 and 0.313, respectively) notably surpass their first-order effects (0.246 and 0.164), confirming that their influence arises predominantly from couplings. Furthermore, the remaining diffusion coefficients (d_{12}, d_{21}, and d_{22}) exhibit high total effects but extremely low first-order effects ($S_1 < 0.2$), indicating they act almost entirely as synergistic catalysts rather than independent drivers.

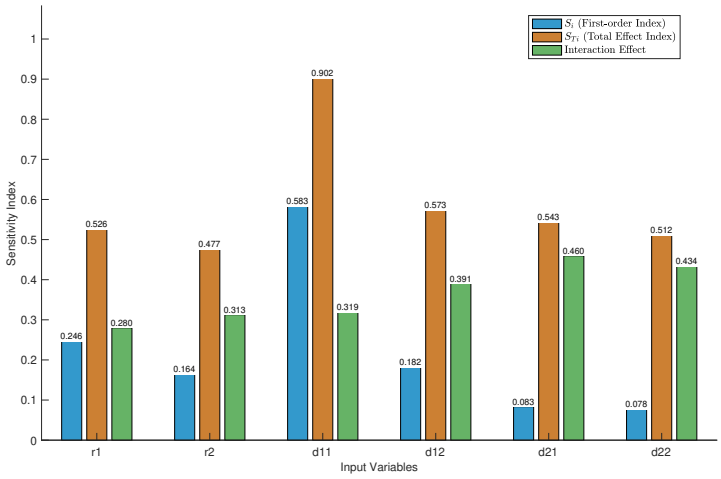

Figure 5. GSA decomposing the first-order, total, and interaction effects of system parameters on mode amplitude ($N = 600$).

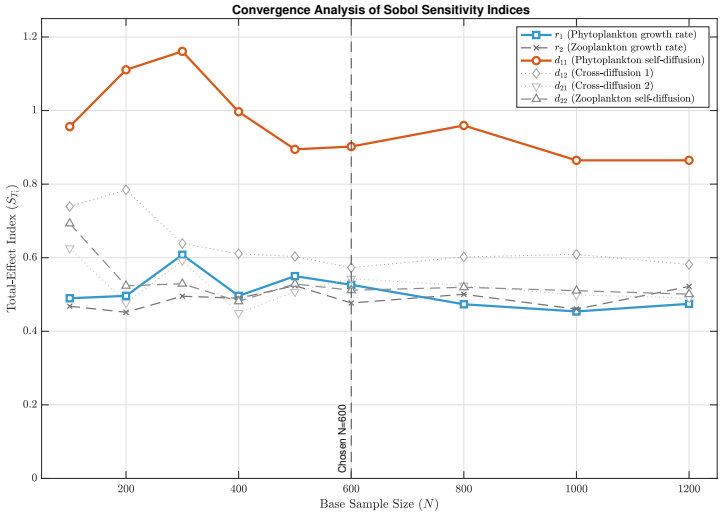

Figure 6. Convergence analysis of Sobol sensitivity indices (S_{T_i}) for six system parameters.

In summary, the system dynamics are primarily driven by d_{11} (the physical anchor for spatial patterning) and r_1 (the core biological engine). In engineering practice, these parameters offer favorable controllability: d_{11} can be modulated via hydrodynamic intervention, while r_1 can be precisely regulated through nutrient enrichment or light-shading strategies. This dominant influence and practical controllability render them optimal control inputs for our adaptive design, which is consistent with other plankton regulation work [25, 38]. Detailed convergence analysis is presented in Figure 6.

5. Optimal control approach

5.1. Formulation of the optimal control problem

System (2.2) describes the spread of phytoplankton and zooplankton in continuous space. In real marine ecological systems, however, interactions often occur on discrete and heterogeneous networks. It is therefore natural to construct a network version of the model so as to describe more realistically the interactions among habitat patches and the resulting dynamical evolution. Since the classical Laplacian operator is defined in continuous space, it is replaced here by the graph Laplacian matrix to capture the discrete network structure.

Consider system (2.2) on a network with N nodes. Let $P_i(t)$ and $Z_i(t)$ denote the phytoplankton and zooplankton densities at node i and time t, respectively. The corresponding uncontrolled baseline networked reaction–diffusion system with time delay is given by

$$\begin{cases} \dfrac{dP_i(t)}{dt} = d_{11}\displaystyle\sum_{j=1}^{N} L_{ij}P_j + d_{12}\sum_{j=1}^{N} L_{ij}Z_j + r_1P_i(t)\left(1-\dfrac{P_i(t)}{\delta}\right) - mf(P_i(t))Z_i(t-\tau), \\ \dfrac{dZ_i(t)}{dt} = d_{21}\displaystyle\sum_{j=1}^{N} L_{ij}P_j + d_{22}\sum_{j=1}^{N} L_{ij}Z_j + r_2Z_i(t)\left(1-\dfrac{Z_i(t)}{\gamma P_i(t)}\right), \end{cases} \tag{5.1}$$

where L_{ij} denotes the (i, j) of the graph Laplacian. This form will be used later when pattern control on networks is discussed.

In this work, we focus on the control of spatial plankton dynamics on complex networks [22, 28], motivated by ecological phenomena such as harmful algal blooms. Traditional control strategies [20, 39] often rely on uniform or empirically chosen weights, which may not adequately reflect the heterogeneous influence of model parameters on system behavior. To address this issue, we develop a sensitivity-guided optimal control framework for a networked reaction-diffusion plankton model with time delay. In this framework, the control is introduced through selected parameters, and a global sensitivity analysis is performed to quantify their relative importance. The resulting model combines delay effects, network structure, and sensitivity-based optimization, providing a quantitative framework for analyzing and controlling spatial plankton patterns.

In particular, the control variables are optimized as node-dependent and time-dependent trajectories over the control horizon. The control objective is twofold:

(i) To minimize the mismatch between the plankton densities and the desired target at time T;
(ii) To balance target attainment against control effort.

To achieve this, we introduce the controlled system where parameters d_{11} and r_1 are upgraded to node-and-time-dependent control variables $d_{11,i}(t)$ and $r_{1,i}(t)$, respectively. Let $P_i(T)$ and $Z_i(T)$ represent the terminal state densities of this controlled system, and the corresponding costate variables $\lambda_{P,i}(t)$ and $\lambda_{Z,i}(t)$ are introduced through the Lagrange multiplier method.

$$\begin{cases} \dfrac{dP_i(t)}{dt} = d_{11,i}\displaystyle\sum_{j=1}^{N} L_{ij}P_j + d_{12}\sum_{j=1}^{N} L_{ij}Z_j + r_{1,i}P_i(t)\left(1 - \dfrac{P_i(t)}{\delta}\right) - mf(P_i(t))Z_i(t-\tau), \\ \dfrac{dZ_i(t)}{dt} = d_{21}\displaystyle\sum_{j=1}^{N} L_{ij}P_j + d_{22}\sum_{j=1}^{N} L_{ij}Z_j + r_2Z_i(t)\left(1 - \dfrac{Z_i(t)}{\gamma P_i(t)}\right). \end{cases} \tag{5.2}$$

The performance index to be minimized is defined by

$$\begin{aligned} J = {} & \frac{1}{2}\sum_{i=1}^{N}\left[\gamma_p(P_i(T) - \bar{P}_i)^2 + \gamma_z(Z_i(T) - \bar{Z}_i)^2\right] \\ & + \frac{1}{2}\int_0^T \sum_{i=1}^{N}\left[\delta_d(d_{11,i}(t) - d_{11,0})^2 + \delta_r(r_{1,i}(t) - r_{1,0})^2\right] dt, \end{aligned} \tag{5.3}$$

where $\bar{P}_i$ and $\bar{Z}_i$ denote the target terminal densities, γ_P and γ_Z denote the weights associated with the terminal tracking error, δ_d and δ_r denote the weights associated with control cost, and $d_{11,0}$ and $r_{1,0}$ denote the baseline values of the control parameters.

5.2. Existence and characterization of the optimal control

To derive the necessary optimality conditions, we employ Pontryagin's maximum principle, as commonly done in pattern-control problems for reaction–diffusion systems [11, 16].

For the network system, we introduce the costate variables $\lambda_{P,i}(t)$ and $\lambda_{Z,i}(t)$ and construct the Lagrangian functional

$$\mathcal{L} = J + \sum_{i=1}^{N} \int_0^T \lambda_{P,i}(t)\left(\frac{dP_i}{dt} - F_{P,i}\right)dt + \sum_{i=1}^{N} \int_0^T \lambda_{Z,i}(t)\left(\frac{dZ_i}{dt} - F_{Z,i}\right)dt,$$

where

$$F_{P,i} = d_{11,i}\sum_{j=1}^{N} L_{ij}P_j + d_{12}\sum_{j=1}^{N} L_{ij}Z_j + r_{1,i}P_i\left(1 - \frac{P_i}{\delta}\right) - m\frac{P_i}{a + P_i}Z_i(t-\tau),$$

$$F_{Z,i} = d_{21}\sum_{j=1}^{N} L_{ij}P_j + d_{22}\sum_{j=1}^{N} L_{ij}Z_j + r_2 Z_i(t)\left(1 - \frac{Z_i}{\gamma P_i}\right).$$

We then define the Hamiltonian

$$H = \frac{1}{2}\sum_{i=1}^{N}\left[\delta_d(d_{11,i}(t) - d_{11,0})^2 + \delta_r(r_{1,i}(t) - r_{1,0})^2\right] + \sum_{i=1}^{N}(\lambda_{P,i}F_{P,i} + \lambda_{Z,i}F_{Z,i}),$$

where $\lambda_{P,i}(t)$ and $\lambda_{Z,i}(t)$ are the costate variables associated with P_i and Z_i, respectively.

The optimal control laws are obtained from the conditions $\partial H/\partial d_{11,i} = 0$ and $\partial H/\partial r_{1,i} = 0$, yielding

$$\frac{\partial H}{\partial d_{11,i}} = \delta_d(d_{11,i} - d_{11,0}) + \lambda_{P,i}\sum_{j=1}^{N} L_{ij}P_j = 0,$$

$$\frac{\partial H}{\partial r_{1,i}} = \delta_r(r_{1,i} - r_{1,0}) + \lambda_{P,i}P_i\left(1 - \frac{P_i}{\delta}\right) = 0.$$

Hence,

$$d_{11,i} = d_{11,0} - \frac{\lambda_{P,i}}{\sum_{j=1}^{N}} L_{ij}P_j\delta_d, \tag{5.4}$$

$$r_{1,i} = r_{1,0} - \frac{\lambda_{P,i}P_i\left(1 - \frac{P_i}{\delta}\right)}{\delta_r}. \tag{5.5}$$

These expressions show that the sensitivity indices directly scale the control adjustments: a higher sensitivity leads to a larger control action for a given costate value, thereby producing a more targeted intervention.

The state equations are

$$\frac{dP_i}{dt} = \frac{\partial H}{\partial \lambda_{P,i}} = F_{P,i},$$

$$\frac{dZ_i}{dt} = \frac{\partial H}{\partial \lambda_{Z,i}} = F_{Z,i},$$

and the costate equations are

$$-\frac{d\lambda_{P,i}}{dt} = \frac{\partial H}{\partial P_i} = \lambda_{P,i}\left[r_{1,i}\left(1-\frac{2P_i}{\delta}\right) - m\frac{a}{(a+P_i)^2}Z_i(t-\tau)\right] + \lambda_{Z,i}\frac{r_2 Z_i^2}{\gamma P_i^2} + \sum_{k=1}^{N}(\lambda_{P,k}L_{ki}d_{11,k} + \lambda_{Z,k}L_{ki}d_{21}), \tag{5.6}$$

$$-\frac{d\lambda_{Z,i}}{dt} = \frac{\partial H}{\partial Z_i} = \lambda_{P,i}\sum_{j=1}^{N}L_{ij}d_{12} + \lambda_{Z,i}\left[r_2\left(1-\frac{2Z_i}{\gamma P_i}\right) + \sum_{j=1}^{N}L_{ij}d_{22}\right] + \mathbb{I}_{\{t\le T-\tau\}}\left[-m\frac{P_i(t+\tau)}{a+P_i(t+\tau)}\lambda_{P,i}(t+\tau)\right], \tag{5.7}$$

where $\mathbb{I}_{\{t\le T-\tau\}}$ is the indicator function associated with the time-delay term.

The boundary conditions are as follows:

(i) Initial conditions:

$$P_i(0) = P_0(1+\varepsilon_i), \qquad Z_i(0) = Z_0(1+\eta_i),$$

where $\varepsilon_i, \eta_i \sim \mathcal{N}(0, 0.01^2)$.

(ii) Terminal conditions:

$$\lambda_{P,i}(T) = \frac{\partial J}{\partial P_i(T)} = \gamma_P(P_i(T) - \bar{P}_i), \tag{5.8}$$

$$\lambda_{Z,i}(T) = \frac{\partial J}{\partial Z_i(T)} = \gamma_Z(Z_i(T) - \bar{Z}_i). \tag{5.9}$$

The state equations, costate equations, optimal control laws, and boundary conditions together form a two-point boundary value problem, whose solution characterizes the optimal control trajectory.

This integrated strategy bridges theoretical control design and empirical parameter importance, and thus offers a scientifically grounded and computationally efficient framework for red tide prevention and ecosystem management.

6. Numerical simulations

6.1. Numerical algorithm and parameter settings

To implement the proposed optimal control strategy and validate the theoretical results, numerical simulations are carried out in this section. The focus is on evaluating the control performance under different network configurations and examining the effect of time delay on the system dynamics.

The network size is set to $N = 1600$, arranged in a 40×40 grid for visualization of spatial patterns. The network topology is generated using Barabási–Albert (BA), Erdős–Rényi (ER), and random regular (RL) models. By varying the network type and its average degree, comparative experiments are conducted. The diffusion coupling is described by the Laplacian matrix L [38]. Time discretization is performed using the explicit Euler scheme, with the total simulation time $T = 40$ and

time step $\Delta t = 2.5 \times 10^{-4}$. The time-delay term is treated via a discrete delay step $k_\tau = \text{round}(\tau/\Delta t)$ by referencing historical state values. Model parameters are taken as in the previous sections, and a scaling factor $s = 0.02$ is introduced for the diffusion coefficients to ensure that the system satisfies the Turing instability condition and generates stable spatial patterns.

In each experiment, the uncontrolled system is first simulated on a given network to obtain its natural spatial pattern. The optimal control strategy is then applied to obtain the controlled pattern. Moreover, the target pattern is generated on a prescribed target network through long-time uncontrolled simulation starting from a perturbed initial condition, and the final steady spatial distribution is extracted as the control objective. The detailed computational procedure is summarized in the following algorithm.

Algorithm 1: GSA-based optimization algorithm for r_1 and d_{11} controls.

Input: Laplacian matrix L; model parameters; delay τ; time step Δt; total steps iterNum; target state P_{target}; lower bound $d_{11}^{\min}$; hyperparameters maxLoop, $\theta, \theta_{\text{tol}}$, relTol.

Output: optimal controls $r_1^{\text{ctrl}}, d_{11}^{\text{ctrl}}$; final objective value $\Im^*$; relative error relErr; terminal state P_{final}.

Step 1: Initialization. Set $r_1^{\text{ctrl}} \leftarrow 0$, $d_{11}^{\text{ctrl}} \leftarrow 0$, $k \leftarrow 1$, and initialize step size θ.

Step 2: Forward simulation. Solve the state system on the network using the explicit Euler scheme:

$$P^{n+1} = P^n + \Delta t \left(d_{11} L P^n + f(P^n, Z^{n-k_\tau}) \right),$$

where $k_\tau = \text{round}(\tau/\Delta t)$ and the delayed variable Z^{n-k_τ} is obtained from stored historical states.

Step 3: Adjoint computation. Solve the adjoint system backward in time using the terminal condition derived from the objective functional.

Step 4: Gradient evaluation. Compute the gradients of the objective functional with respect to r_1^{ctrl} and d_{11}^{ctrl} based on the state and adjoint variables.

Step 5: Control update. Update the controls using gradient descent:

$$r_1^{\text{ctrl}} \leftarrow r_1^{\text{ctrl}} - \theta \nabla_{r_1} \Im, \quad d_{11}^{\text{ctrl}} \leftarrow \max\left(d_{11}^{\min},\, d_{11}^{\text{ctrl}} - \theta \nabla_{d_{11}} \Im \right).$$

Step 6: Convergence check. Recompute the state system and evaluate relErr. If relErr < relTol or $k \geq$ maxLoop, stop; otherwise update θ if necessary, set $k \leftarrow k + 1$, and repeat Steps 2–5.

Step 7: Output. Set $\Im^* \leftarrow \Im$ and $P_{\text{final}} \leftarrow P(:, \text{end})$.

6.2. Verification of optimal control effectiveness

In practical ecological management, the ability to regulate spatial patterns is crucial for preventing harmful algal blooms such as red tides. In this section, the effectiveness of the proposed optimal control strategy is examined under different network configurations. Three types of experiments are performed:

(i) Control under the same network topology with different average degrees;
(ii) Control between different network topologies with the same average degree;
(iii) Control between networks with both different topology and different average degree.

All cases (Case A to Case C) below adopt the computational procedure summarized in Algorithm 1. To quantitatively evaluate the performance of the proposed optimal control method, the

objective functional and relative error are defined as:

$$\Im = \frac{1}{2}\sum_{i=1}^{N}\left(P_i(T) - P_i^{\text{target}}\right)^2, \quad \text{relErr}(P) = \frac{\|P^{\text{final}} - P^{\text{target}}\|_2}{\|P^{\text{target}}\|_2}. \tag{6.1}$$

Case A. Control with different average degrees in the same network type.

First, the control performance is tested on BA networks with different average degrees. Starting from an initial network configuration, the proposed optimal control method is applied to guide the system toward target networks with increasing connectivity.

The BA network represents a scale-free natural ecosystem, where increasing the average degree improves habitat connectivity. For the three scenarios BA20→BA30, BA20→BA80, and BA20→BA140, the objective function values are 9.85572, 5.42307, and 5.77692, with relative errors of 3.335×10^{-2}, 2.082×10^{-2}, and 1.780×10^{-2}, respectively. As shown in Figure 8, a larger average degree leads to stronger diffusion coupling between nodes, smaller control error, and higher control precision, thereby facilitating faster convergence to the desired spatial pattern. Thus, appropriately improving habitat connectivity optimizes the regulation effect.

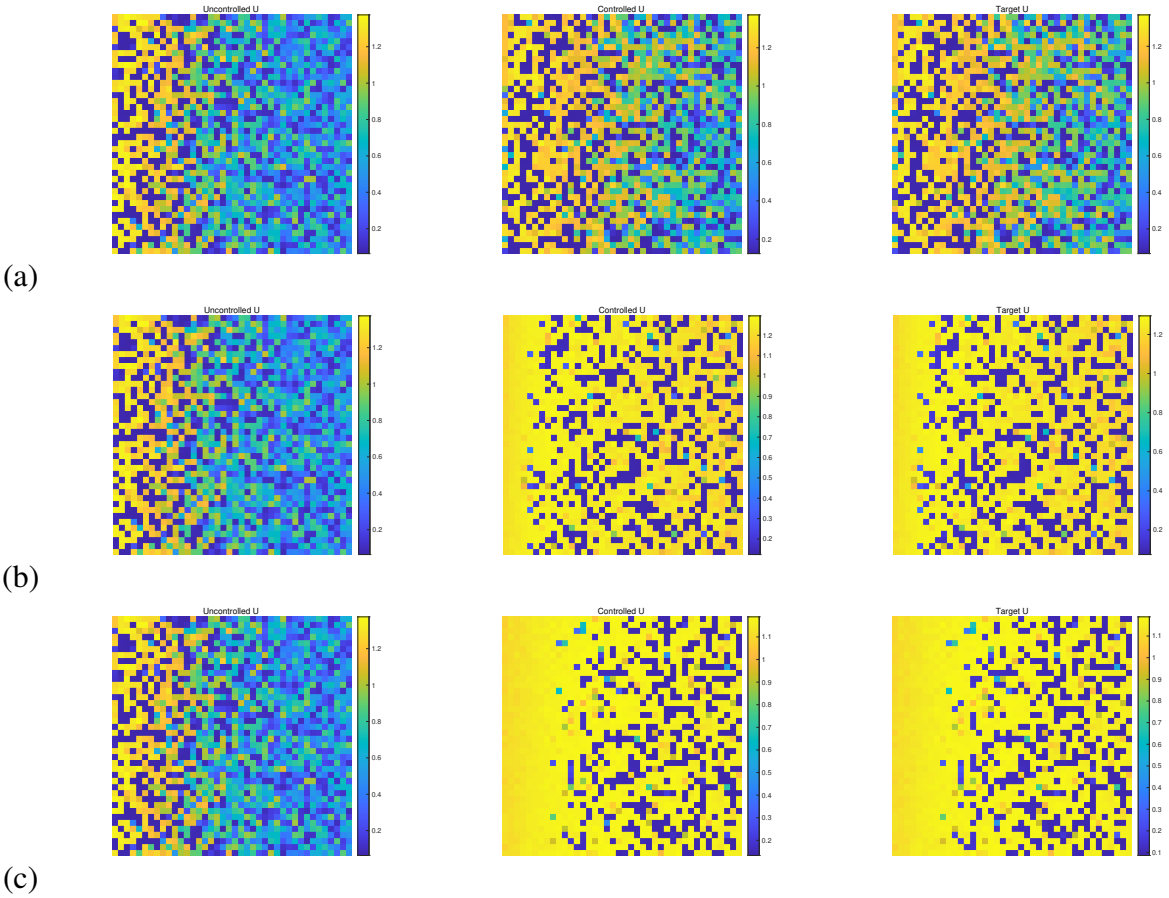

Figure 7. Pattern transition for BA networks with different average degrees: (a) BA20 → BA30:$\Im = 9.85572, relErr(P) = 3.335 \times 10^{-2}$, (b) BA20 → BA80:$\Im = 5.42307, relErr(P) = 2.082 \times 10^{-2}$, (c) BA20 → BA140:$\Im = 5.77692, relErr(P) = 1.780 \times 10^{-2}$.

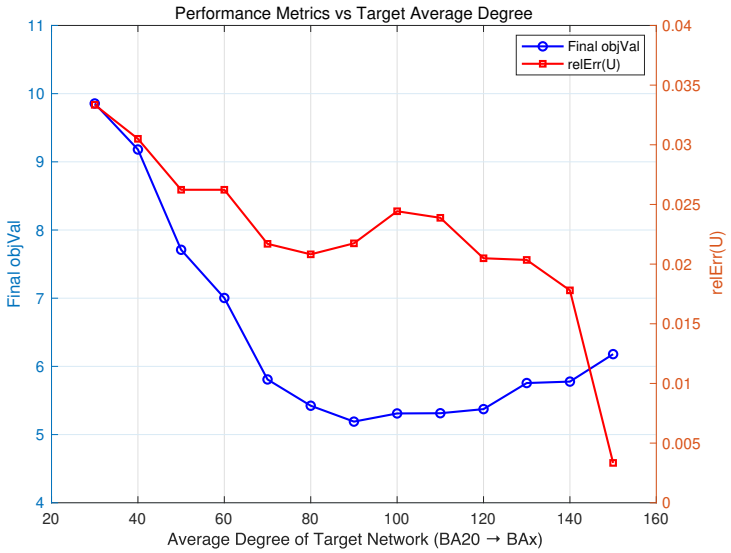

Figure 8. Dependence of performance metrics on the average degree of the target network.

Case B. Control between different network topologies with the same average degree.

In realistic marine ecosystems, spatial connectivity is often determined by hydrodynamic transport processes and biological migration pathways. These processes may lead to different network structures even when the overall connectivity strength is similar.

To investigate the adaptability of the proposed control method, three types of network structures are considered: RL, BA network, and ER network [22]. In this experiment, the average degree of the networks is kept constant while the topology changes. This comparison is motivated by other studies on complex networks, community structures, and network-organized pattern dynamics. Figures 9 and 10 present the spatial pattern transition between network structures.

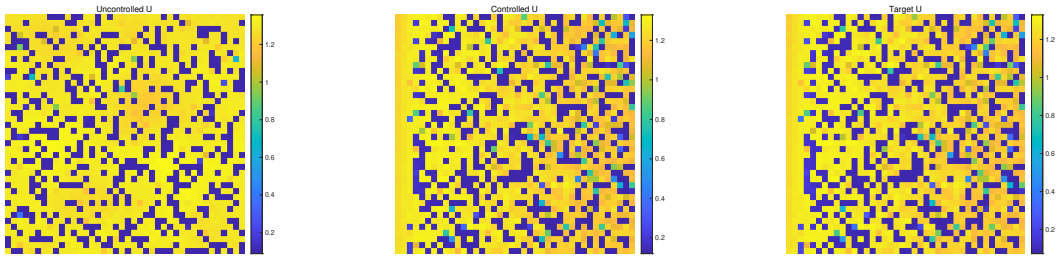

Figure 9. Spatial pattern transition between network structures with the same average degree: RL60 → BA60: $\Im = 6.8954, relErr(P) = 2.238 \times 10^{-2}$. The three panels show the uncontrolled pattern, target pattern, and controlled pattern.

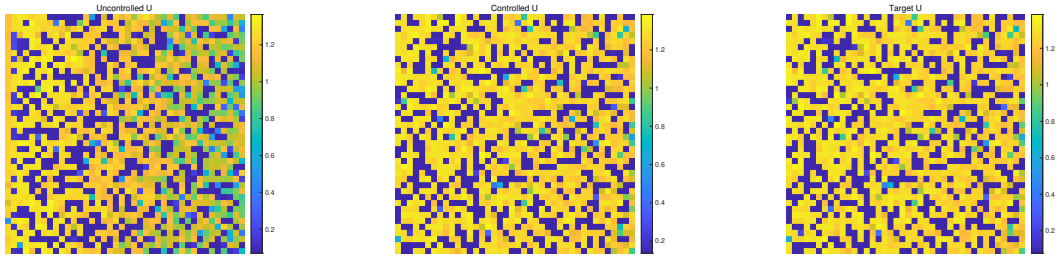

Figure 10. Spatial pattern transition between network structures with the same average degree: BA40 → ER40: $\Im = 7.31149, relErr(P) = 3.077 \times 10^{-2}$. The three panels show the uncontrolled pattern, target pattern, and controlled pattern.

Even when the average degree is fixed, different network topologies still generate markedly different spatial patterns. The numerical results show that the proposed control strategy can effectively realize pattern transitions across networks. The average relative error is 2.238% from RL60 to BA60 and 3.077% from BA40 to ER40, while the final objective value rises from below 3.5% in case1 to 7%, indicating that the control difficulty increases for cross-topology regulation. In ecological terms, the larger error may be associated with the dominant transport role of hub nodes in scale-free networks, which makes recovery from heterogeneous to more regular diffusion structures more difficult.

Case C. Control between networks with different topology and connectivity.

In real plankton ecosystems, spatial coupling among habitats is determined not only by the topology of transport pathways but also by the overall strength of hydrodynamic connectivity. Diffusion, mixing, and advection can therefore generate substantially different spatial interaction patterns among regions. For example, local diffusion and short-range mixing typically produce neighborhood-dominated coupling structures that can be represented by regular or lattice-like networks, whereas strong transport corridors may generate heterogeneous connections similar to scale-free networks, and highly mixed environments may result in more random interaction patterns. It is therefore ecologically meaningful to examine pattern regulation under simultaneous changes in topology and connectivity strength in light of modern network representations. Figures 11 and 12 illustrate the spatial pattern transition under such conditions.

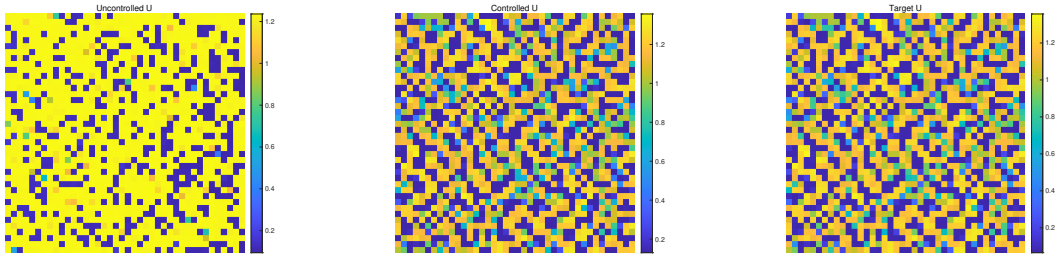

Figure 11. Pattern transition between networks with different topology and average degree: ER100 → RL24:$\Im = 12.3274, relErr(P) = 4.192 \times 10^{-2}$.

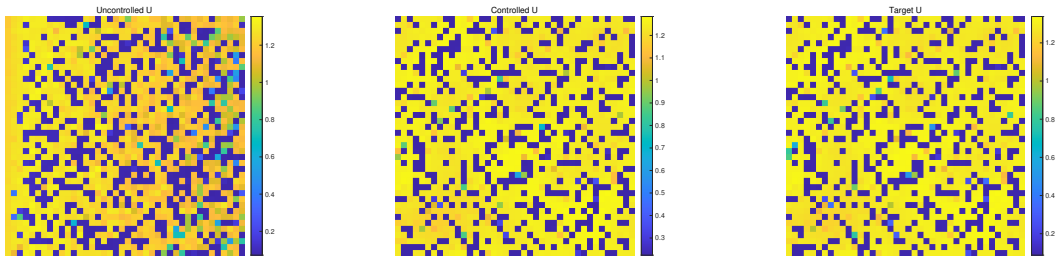

Figure 12. Pattern transition between networks with different topology and average degree: BA50 → RL60:$\Im = 9.08724, relErr(P) = 7.648 \times 10^{-2}$.

This corresponds to the disturbance scenario where the habitat connection mode and connectivity of the ecological system change simultaneously. In the scenarios of ER100→RL24 and BA50→RL60, the objective function values are 12.3274 and 9.08724, respectively, with relative errors of 4.192×10^{-2} and 7.648×10^{-2}. The regularity conclusion is: With the simultaneous changes in the topological structure and average degree of the ecological network, the difficulty of system regulation gradually increases, but the proposed method can still stabilize the control error below 8%, showing excellent robustness.

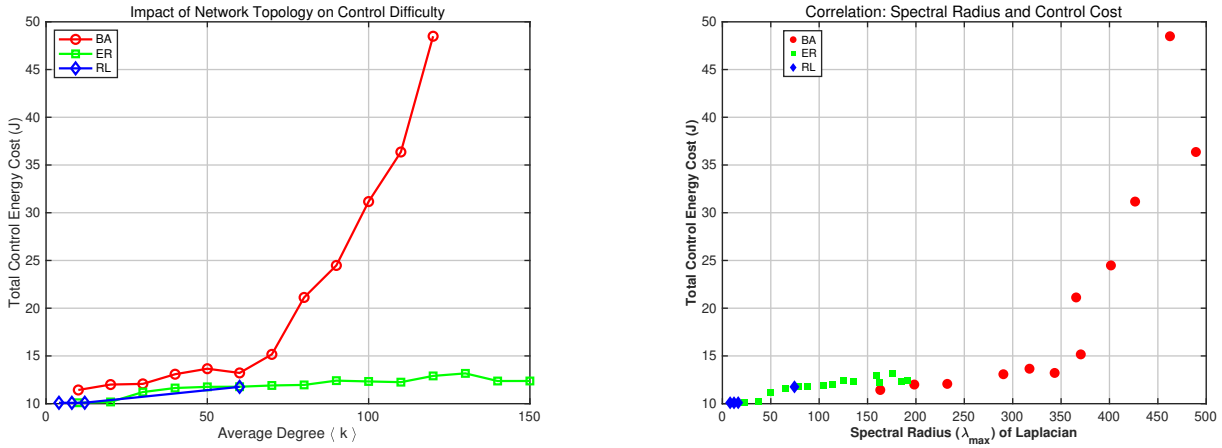

Figure 13. Relationship between total control energy cost and network characteristic parameters. Left: Control cost versus average degree $\langle k \rangle$; Right: Control cost versus spectral radius of Laplacian $\lambda_{\max}$.

To further explore the effects of network topology on control performance, we take control energy consumption as the evaluation index and analyze the regulation performance of the system under different topological structures and connectivity strengths. The average degree determines the exchange efficiency of substances and populations between nodes, while the Laplacian spectral radius characterizes the dynamic coupling strength of the system. Both indicators exert remarkable impacts on control cost. The experimental results show that RL regular networks and ER random networks possess homogeneous structures, whose system states can be corrected with relatively low control energy consumption. In contrast, the dynamic evolution of BA scale-free networks is dominated by hub nodes, leading to strong spatiotemporal correlation and greatly increasing the difficulty of

regulating spatial patterns. This result quantitatively clarifies the internal relationships among topology, dynamic characteristics, and control difficulty, and provides experimental support for the design of the sensitivity-guided optimal control strategy proposed in this paper.

6.3. *Effect of time delay on control performance*

To investigate the influence of time delay on control performance, we conduct error comparison experiments. Taking the ER50→RL60 network as an example, we further introduce a classical proportional feedback control as a benchmark for comparison. Specifically, the classical control inputs are designed as

$$r_1 = K_p^{(1)}(P^* - P), \quad d_{11} = K_p^{(2)}|Z^* - Z|, \tag{6.2}$$

where P^* and Z^* denote the target states, and $K_p^{(1)}$, $K_p^{(2)}$ are constant feedback gains. The comparison results between the uncontrolled case, the classical control, and the proposed optimal control strategy are shown in Figure 14.

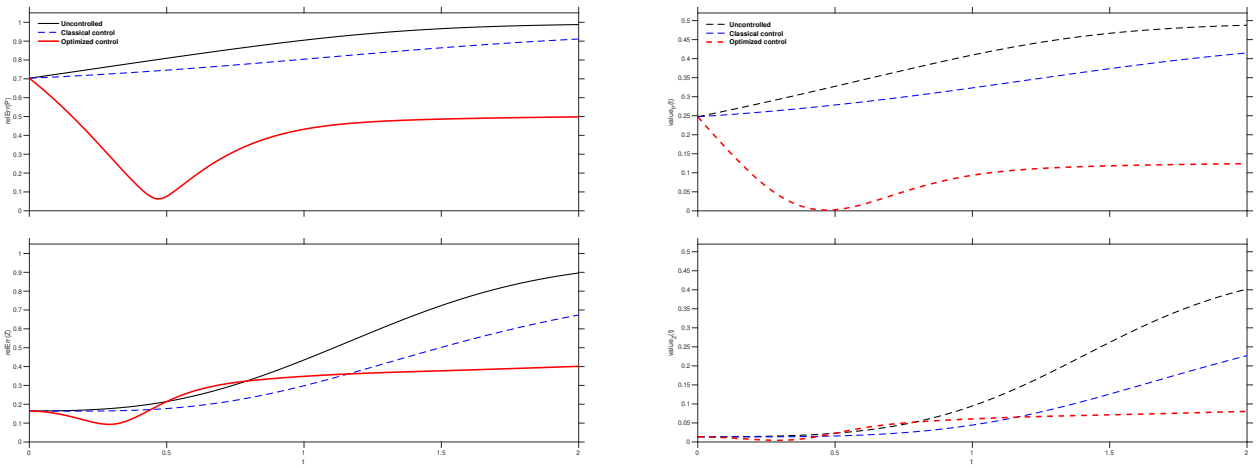

Figure 14. Comparison of control performance under delay $\tau = 0.8$ over a time horizon $T = 2$. The left panel shows the relative errors of P and Z, while the right panel presents the corresponding value functions.

To systematically investigate the quantitative relationship between the time-delay thresholds and the resulting control performance, Table 3 summarizes the tracking precision and objective valuations across a dense spectrum of landmark boundaries from $\tau = 0.3$ to $\tau = 0.8$. For the uncontrolled and classical feedback baseline groups, a prominent monotonic degradation trend is observable: As the feedback lag expands, the terminal residual tracking errors (*relErr*) and the value function costs (*val*) grow monotonically, which explicitly confirms the severe perturbation of the delay threshold on the system's native stability. Conversely, the proposed sensitivity-guided optimal control maintains an exceptionally stable performance boundary, consistently regulating the terminal relative errors around a level of 0.48 across all tested thresholds and demonstrating remarkable structural robustness.

The robust performance of the proposed control framework, exhibiting no significant sensitivity to time delays, could be attributed to several core factors, including the morphogenetic nature of the pattern-to-pattern transition task, the multi-objective Pareto trade-off, and the structural decoupling

enabled by the dominant spatial diffusion channel. This conclusion is also laterally supported from a fundamental mathematical perspective by related literature [40, 41].

Table 3. Quantitative control performance and tracking precision under distinct landmark time-delay thresholds ($T = 2.0$).

Delay (τ)	Control Scheme	$relErr(P)$	$relErr(Z)$	val_P	val_Z
$\tau = 0.3$	Uncontrolled	0.9685	0.8121	0.4690	0.3298
	Classical P-Control	0.8722	0.6034	0.3804	0.1821
	Sensitivity-Guided Optimal	**0.4819**	**0.4579**	**0.1161**	**0.1049**
$\tau = 0.4$	Uncontrolled	0.9736	0.8334	0.4740	0.3472
	Classical P-Control	0.8815	0.6215	0.3885	0.1931
	Sensitivity-Guided Optimal	**0.4810**	**0.4608**	**0.1157**	**0.1062**
$\tau = 0.5$	Uncontrolled	0.9782	0.8528	0.4785	0.3637
	Classical P-Control	0.8903	0.6384	0.3963	0.2038
	Sensitivity-Guided Optimal	**0.4800**	**0.4635**	**0.1152**	**0.1074**
$\tau = 0.6$	Uncontrolled	0.9822	0.8700	0.4823	0.3784
	Classical P-Control	0.8983	0.6536	0.4035	0.2136
	Sensitivity-Guided Optimal	**0.4788**	**0.4662**	**0.1146**	**0.1087**
$\tau = 0.7$	Uncontrolled	0.9853	0.8846	0.4854	0.3912
	Classical P-Control	0.9053	0.6669	0.4098	0.2224
	Sensitivity-Guided Optimal	**0.4774**	**0.4691**	**0.1139**	**0.1100**
$\tau = 0.8$	Uncontrolled	0.9878	0.8965	0.4879	0.4019
	Classical P-Control	0.9114	0.6781	0.4153	0.2299
	Sensitivity-Guided Optimal	**0.4757**	**0.4722**	**0.1131**	**0.1115**

In summary, the proposed sensitivity-guided optimal control strategy can effectively regulate the spatial dynamics of the plankton ecosystem due to its low-sensitivity characteristics to delay variations. The method maintains strong robustness when facing system delays and structural changes, providing a reliable quantitative tool for the regulation and management of complex marine ecological systems.

7. Conclusions

In this paper, we investigate the formation and control of spatial patterns in plankton ecosystems. We construct a network-based reaction–diffusion model incorporating time delay and cross-diffusion. In this framework, each network node represents a local habitat patch, and the coupling between nodes describes material exchange and biological migration, enabling the model to more realistically capture the spatiotemporal dynamics of plankton populations in complex environments.

Theoretical analysis shows that diffusion drives the formation of Turing patterns, while time delay induces temporal oscillations. Through linear stability analysis and the discussion of Turing and Hopf instabilities, the mechanisms underlying plankton patchiness and periodic outbreaks such as red tides can be explained from a dynamical perspective. These results reveal the intrinsic instability of the ecosystem and highlight the need of introducing control mechanisms.

On this basis, we further study how to effectively regulate such complex ecological dynamics.

Different from traditional classical control methods, we introduce GSA, where the FFT amplitude of spatial patterns is used as a quantitative indicator to identify the most influential parameters, namely d_{11} and r_1. In the optimal control formulation, these key parameters are treated as control variables, and node-dependent and time-dependent dynamic optimal controls are implemented. In this way, more targeted regulation can be achieved.

Numerical results show that the proposed control strategy exhibits good adaptability under different network structures and connectivity strengths. Even when the network topology and average degree vary simultaneously, the system can still be effectively driven toward the desired spatial pattern, with the average relative error maintained below 8%. Moreover, although time delay tends to weaken system stability and induce oscillatory behavior, the proposed control method can significantly reduce the system deviation in the short term and maintain better performance over longer time horizons, thereby mitigating the adverse effects of delay to some extent.

In conclusion, ecological connectivity and intrinsic system dynamics jointly determine the formation and evolution of spatial patterns, while regulation based on key parameters can effectively influence this process. The proposed modeling and control framework provides a quantitative tool for understanding spatial heterogeneity in plankton ecosystems and offers potential insights for the prediction and management of ecological phenomena such as red tides.

Although the current modeling framework serves as a reasonable and idealized approximation that successfully balances ecological fidelity with control-theoretic tractability, researchers can proceed in several directions to further refine and granularize the system. On the one hand, the model can be extended to more complex high-order dynamical systems, such as multi-variable coupled systems, nonlocal diffusion, and more general network structures, to better capture real-world complexity. On the other hand, incorporating observational or statistical data for parameter calibration would improve the interpretability and predictive capability of the model. However, such developments require extensive data support and systematic validation, and therefore remain topics for future investigation.

Use of AI tools declaration

The authors declare they have not used Artificial Intelligence (AI) tools in the creation of this article.

Conflict of interest

The authors declare there are no conflicts of interest.

References

1. J. Nabe-Nielsen, F. M. van Beest, V. Grimm, R. M. Sibly, J. Teilmann, P. M. Thompson, Predicting the impacts of anthropogenic disturbances on marine populations, *Conserv. Lett.*, **11** (2018), e12563. https://doi.org/10.1111/conl.12563

2. L. N. de S. Domis, J. J. Elser, A. S. Gsell, V. L. M. Huszar, B. W. Ibelings, E. Jeppesen, et al., Plankton dynamics under different climatic conditions in space and time, *Freshwater Biol.*, **58** (2013), 463–482. https://doi.org/10.1111/fwb.12053

3. D. G. George, S. I. Heaney, Factors influencing the spatial distribution of phytoplankton in a small productive lake, *J. Ecol.*, **66** (1978), 133–155. https://doi.org/10.2307/2259185
4. J. Song, C. Hou, Q. Liu, X. Wu, Y. Wang, Y. Yi, Spatial and temporal variations in the plankton community because of water and sediment regulation in the lower reaches of Yellow River, *J. Cleaner Prod.*, **261** (2020), 120972. https://doi.org/10.1016/j.jclepro.2020.120972
5. G. P. Harris, *Phytoplankton Ecology: Structure, Function and Fluctuation*, Springer, 1986. https://doi.org/10.1007/978-94-009-4081-9
6. K. Dehingia, A. Das, E. Hinçal, K. Hosseini, The effect of time delay on the dynamics of a plankton-nutrient system with refuge, *Braz. J. Phys.*, **55** (2025), 28. https://doi.org/10.1007/s13538-024-01670-0
7. A. B. Medvinsky, I. A. Tikhonova, B. L. Li, H. Malchow, Time delay as a key factor of model plankton dynamics, *C.R. Biol.*, **327** (2004), 277–282. https://doi.org/10.1016/j.crvi.2003.11.013
8. I. Lengyel, I. R. Epstein, A chemical approach to designing Turing patterns in reaction-diffusion systems, *Proc. Natl. Acad. Sci. U.S.A.*, **89** (1992), 3977–3979. https://doi.org/10.1073/pnas.89.9.3977
9. H. Nakao, A. S. Mikhailov, Turing patterns in network-organized activator–inhibitor systems, *Nat. Phys.*, **6** (2010), 544–550. https://doi.org/10.1038/nphys1651
10. J. Shi, L. Zhu, Turing pattern theory on homogeneous and heterogeneous higher-order temporal network system, *J. Math. Phys.*, **66** (2025), 042706. https://doi.org/10.1063/5.0211728
11. X. Yu, S. Yuan, T. Zhang, Survival and ergodicity of a stochastic phytoplankton-zooplankton model with toxin-producing phytoplankton in an impulsive polluted environment, *Appl. Math. Comput.*, **347** (2019), 249–264. https://doi.org/10.1016/j.amc.2018.11.005
12. H. Liu, C. Dai, H. Yu, Q. Guo, J. Li, A. Hao, et al., Dynamics of a stochastic non-autonomous phytoplankton-zooplankton system involving toxin-producing phytoplankton and impulsive perturbations, *Math. Comput. Simul.*, **203** (2023), 368–386. https://doi.org/10.1016/j.matcom.2022.06.012
13. W. Wang, S. Liu, Z. Liu, D. Wang, Pattern dynamics in a predator-prey model with schooling behavior and cross-diffusion, *Int. J. Bifurcation Chaos*, **29** (2019), 1950146. https://doi.org/10.1142/S0218127419501463
14. P. K. Tiwari, S. Roy, A. K. Misra, R. K. Upadhyay, Effect of seasonality on a nutrient–plankton system with toxicity in the presence of refuge and additional food, *Eur. Phys. J. Plus*, **137** (2022), 368. https://doi.org/10.1140/epjp/s13360-022-02566-1
15. M. Rehim, M. Imran, Dynamical analysis of a delay model of phytoplankton–zooplankton interaction, *Appl. Math. Modell.*, **36** (2012), 638–647. https://doi.org/10.1016/j.apm.2011.07.018
16. N. F. Britton, *Reaction-Diffusion Equations and Their Applications to Biology*, Academic Press, Orlando, 1986.
17. X. Shao, Y. Fang, B. Cui, A model to evaluate spatiotemporal variations of hydrological connectivity on a basin-scale complex river network with intensive human activity, *Sci. Total Environ.*, **723** (2020), 138051. https://doi.org/10.1016/j.scitotenv.2020.138051

18. M. M. Silvestrini, N. W. Smith, A. J. Fletcher, W. C. McNabb, F. M. Sarti, Complex network analysis and health implications of nutrient trade, *Global Food Secur.*, **40** (2024), 100743. https://doi.org/10.1016/j.gfs.2024.100743

19. A. Deutsch, P. Friedl, L. Preziosi, G. Theraulaz, Multi-scale analysis and modelling of collective migration in biological systems, *Phil. Trans. R. Soc. B*, **375** (2020), 20190377. https://doi.org/10.1098/rstb.2019.0377

20. L. Chang, S. Gao, Z. Wang, Optimal control of pattern formations for an SIR reaction-diffusion epidemic model, *J. Theor. Biol.*, **536** (2022), 111003. https://doi.org/10.1016/j.jtbi.2022.111003

21. L. Zhu, Y. Ding, S. Shen, Green behavior propagation analysis based on statistical theory and intelligent algorithm in data-driven environment, *Math. Biosci.*, **379** (2025), 109340. https://doi.org/10.1016/j.mbs.2025.109340

22. L. Zhu, L. He, Pattern dynamics analysis and parameter identification of time delay-driven rumor propagation model based on complex networks, *Nonlinear Dyn.*, **110** (2022), 1935–1957. https://doi.org/10.1007/s11071-022-07717-8

23. R. Balderrama, M. I. Prieto, C. S. de la Vega, F. Vázquez, Optimal control for an SIR model with limited hospitalised patients, *Math. Biosci.*, **378** (2024), 109317. https://doi.org/10.1016/j.mbs.2024.109317

24. Z. Jiang, M. Jie, Bifurcation control of a minimal model of marine plankton interaction with multiple delays, *Math. Modell. Nat. Phenom.*, **16** (2021), 16. https://doi.org/10.1051/mmnp/2021013

25. Y. Lu, M. Xiao, J. Liang, J. Ding, Y. Zhou, Y. Wan, et al., Hybrid control synthesis for Turing instability and Hopf bifurcation of marine planktonic ecosystems with diffusion, *IEEE Access*, **9** (2021), 111326–111335. https://doi.org/10.1109/ACCESS.2021.3103446

26. J. Li, Y. Song, H. Wan, H. Zhu, Dynamical analysis of a toxin-producing phytoplankton-zooplankton model with refuge, *Math. Biosci. Eng.*, **14** (2017), 529–557. https://doi.org/10.3934/mbe.2017032

27. J. A. Freund, S. Mieruch, B. Scholze, K. H. Wiltshire, U. Feudel, Bloom dynamics in a seasonally forced phytoplankton-zooplankton model: trigger mechanisms and timing effects, *Ecol. Complexity*, **3** (2006), 129–139. https://doi.org/10.1016/j.ecocom.2005.11.001

28. B. Li, L. Zhu, Turing instability analysis of a reaction–diffusion system for rumor propagation in continuous space and complex networks, *Inf. Process. Manage.*, **61** (2024), 103621. https://doi.org/10.1016/j.ipm.2023.103621

29. Y. Wang, F. Song, J. Zhu, S. Zhang, Y. Yang, T. Chen, et al., GSA: genome sequence archive, *Genomics Proteomics Bioinf.*, **15** (2017), 14–18. https://doi.org/10.1016/j.gpb.2017.01.001

30. C. Wang, N. Li, Propagation dynamics of malware in wireless sensor networks with node sleep-active scheduling based on simplicial complexes, *Phys. Scr.*, **101** (2026), 075206. https://doi.org/10.1088/1402-4896/ae41f2

31. R. Zhou, N. N. B. Mansor, H. A. Illias, Identification of inrush current using a GSA-BP network, *Energies*, **16** (2023), 2340. https://doi.org/10.3390/en16052340

32. Q. Ding, N. Li, The challenges of medical resource limitations for tuberculosis under the COVID-19 pandemic: A mathematical modeling of co-infection and optimal control, *J. Biol. Syst.*, **32** (2024), 1003–1038. https://doi.org/10.1142/S0218339024500335
33. W. Wang, S. Liu, Z. Liu, Spatiotemporal dynamics near the Turing-Hopf bifurcation in a toxic-phytoplankton–zooplankton model with cross-diffusion, *Nonlinear Dyn.*, **98** (2019), 27–37. https://doi.org/10.1007/s11071-019-05168-2
34. C. S. Holling, The components of predation as revealed by a study of small-mammal predation of the European pine sawfly, *Can. Entomol.*, **91** (1959), 293–320. https://doi.org/10.4039/Ent91293-5
35. M. M. Mullin, E. F. Stewart, F. J. Fuglister, Ingestion by planktonic grazers as a function of concentration of food, *Limnol. Oceanogr.*, **20** (1975), 259–262. https://doi.org/10.4319/lo.1975.20.2.0259
36. M. J. R. Fasham, H. W. Ducklow, S. M. McKelvie, A nitrogen-based model of plankton dynamics in the oceanic mixed layer, *J. Mar. Res.*, **48** (1990), 591–639.
37. W. Gentleman, A. Leising, B. Frost, S. Strom, J. Murray, Functional responses for zooplankton feeding on multiple resources: a review of assumptions and biological dynamics, *Deep Sea Res. Part II*, **50** (2003), 2847–2875. https://doi.org/10.1016/j.dsr2.2003.07.001
38. S. Gao, L. Chang, I. Romić, Z. Wang, M. Jusup, P. Holme, Optimal control of networked reaction–diffusion systems, *J. R. Soc. Interface*, **19** (2022), 20210739. https://doi.org/10.1098/rsif.2021.0739
39. S. Temel, S. Yağli, S. P. Gören, *P, PD, PI, PID Controllers*, 2013
40. S. T. Vittadello, T. Leyshon, D. Schnoerr, M. P. H. Stumpf, Turing pattern design principles and their robustness, *Phil. Trans. R. Soc. A*, **379** (2021), 20200272. https://doi.org/10.1098/rsta.2020.0272
41. Q. Zhang, Pareto optimality under H_∞ constraint for linear delayed stochastic systems in finite horizon, in *2024 43rd Chinese Control Conference (CCC)*, (2024), 1699–1704. https://doi.org/10.23919/CCC63176.2024.10662397

AIMS Press